24. COSMIC RAYS

Revised August 2007 by T.K. Gaisser and T. Stanev (Bartol Research Inst., Univ. of Delaware).

24.1. Primary spectra

The cosmic radiation incident at the top of the terrestrial atmosphere includes all stable charged particles and nuclei with lifetimes of order 10^6 years or longer. Technically, "primary" cosmic rays are those particles accelerated at astrophysical sources, and "secondaries" are those particles produced in interaction of the primaries with interstellar gas. Thus, electrons, protons, and helium, as well as carbon, oxygen, iron, and other nuclei synthesized in stars, are primaries. Nuclei such as lithium, beryllium, and boron (which are not abundant end-products of stellar nucleosynthesis) are secondaries. Antiprotons and positrons are also in large part secondary. Whether a small fraction of these particles may be primary is a question of current interest.

Apart from particles associated with solar flares, the cosmic radiation comes from outside the solar system. The incoming charged particles are "modulated" by the solar wind, the expanding magnetized plasma generated by the Sun, which decelerates and partially excludes the lower energy galactic cosmic rays from the inner solar system. There is a significant anticorrelation between solar activity (which has an alternating eleven-year cycle) and the intensity of the cosmic rays with energies below about 10 GeV. In addition, the lower-energy cosmic rays are affected by the geomagnetic field, which they must penetrate to reach the top of the atmosphere. Thus the intensity of any component of the cosmic radiation in the GeV range depends both on the location and time.

There are four different ways to describe the spectra of the components of the cosmic radiation: (1) By particles per unit rigidity. Propagation (and probably also acceleration) through cosmic magnetic fields depends on gyroradius or *magnetic rigidity,* R, which is gyroradius multiplied by the magnetic field strength:

$$R = \frac{p\,c}{Z\,e} = r_{_L} B \ . \tag{24.1}$$

(2) By particles per energy-per-nucleon. Fragmentation of nuclei propagating through the interstellar gas depends on energy per nucleon, since that quantity is approximately conserved when a nucleus breaks up on interaction with the gas. (3) By nucleons per energy-per-nucleon. Production of secondary cosmic rays in the atmosphere depends on the intensity of nucleons per energy-per-nucleon, approximately independently of whether the incident nucleons are free protons or bound in nuclei. (4) By particles per energy-per-nucleus. Air shower experiments that use the atmosphere as a calorimeter generally measure a quantity that is related to total energy per particle.

The units of differential intensity I are $[\mathrm{m}^{-2}\,\mathrm{s}^{-1}\mathrm{sr}^{-1}\mathcal{E}^{-1}]$, where $\mathcal{E}$ represents the units of one of the four variables listed above.

The intensity of primary nucleons in the energy range from several GeV to somewhat beyond 100 TeV is given approximately by

$$I_N(E) \ \approx \ 1.8 \times 10^4 \ (E/1\ \mathrm{GeV})^{-\alpha} \ \frac{\mathrm{nucleons}}{\mathrm{m}^2\ \mathrm{s}\ \mathrm{sr}\ \mathrm{GeV}} \ , \tag{24.2}$$

where E is the energy-per-nucleon (including rest mass energy), and α $(\equiv \gamma + 1) = 2.7$ is the differential spectral index of the cosmic ray flux and γ is the integral spectral index. About 79% of the primary nucleons are free protons and about 70% of the rest are nucleons bound in helium nuclei. The fractions of the primary nuclei are nearly constant over this energy range (possibly with small but interesting variations). Fractions of both primary and secondary incident nuclei are listed in Table 24.1. Figure 24.1 shows the major components for energies greater than 2 GeV/nucleon.

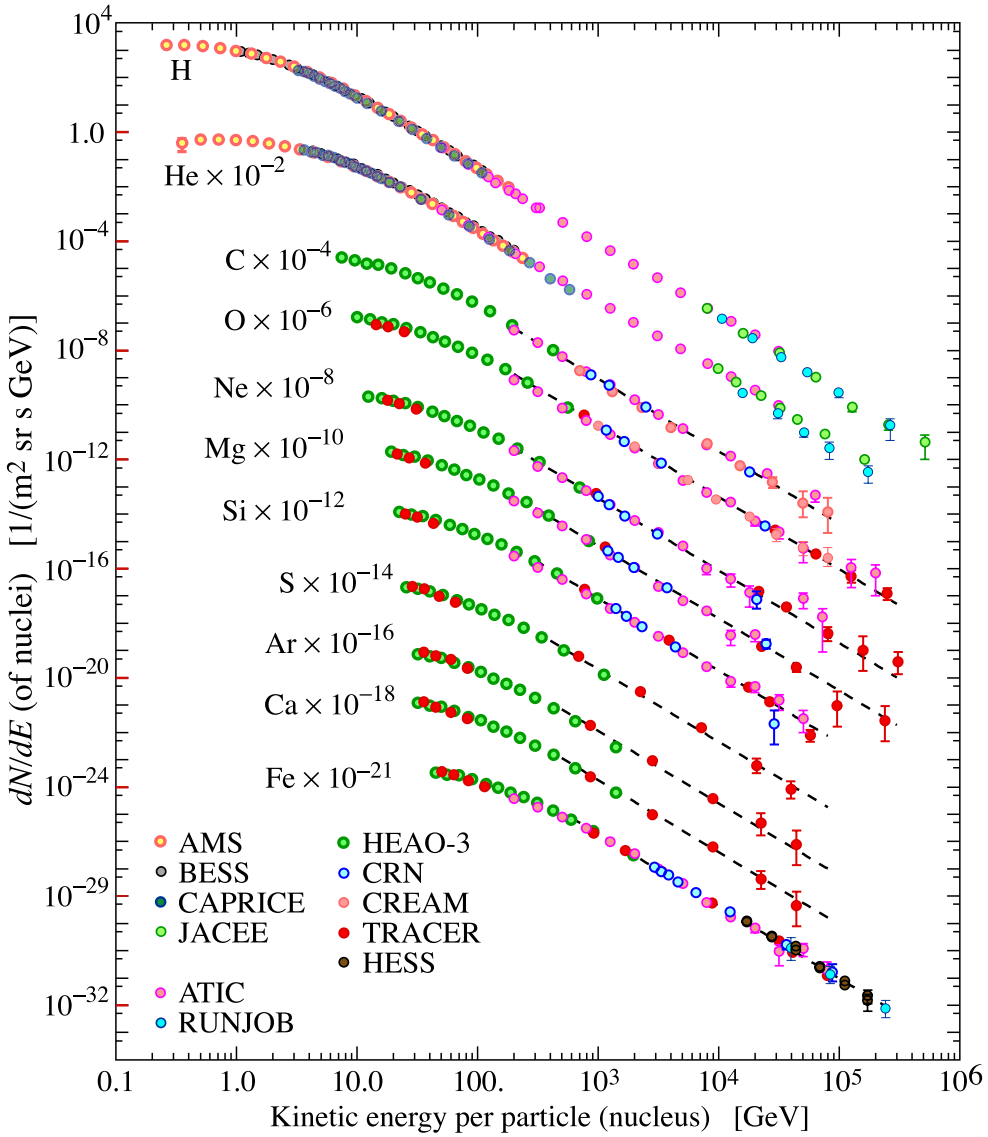

Figure 24.1: Major components of the primary cosmic radiation from Refs. [1–12]. The figure was created by P. Boyle and D. Muller.

The composition and energy spectra of nuclei are typically interpreted in the context of propagation models, in which the sources of the primary cosmic radiation are located within the galaxy [13]. The ratio of secondary to primary nuclei is observed to decrease

Table 24.1: Relative abundances F of cosmic-ray nuclei at 10.6 GeV/nucleon normalized to oxygen ($\equiv 1$) [6]. The oxygen flux at kinetic energy of 10.6 GeV/nucleon is 3.26×10^{-6} cm^{-2} s^{-1} sr^{-1} (GeV/nucleon)$^{-1}$. Abundances of hydrogen and helium are from Refs. [2,3]. Note that one can not use these values to extend the cosmic ray flux to high energy because the power law spectrum is not fully established yet and that Figure 24.1 is in energy per particle.

Z	Element	F	Z	Element	F
1	H	540	13–14	Al-Si	0.19
2	He	26	15–16	P-S	0.03
3–5	Li-B	0.40	17–18	Cl-Ar	0.01
6–8	C-O	2.20	19–20	K-Ca	0.02
9–10	F-Ne	0.30	21–25	Sc-Mn	0.05
11–12	Na-Mg	0.22	26–28	Fe-Ni	0.12

with increasing energy, a fact interpreted to mean that the lifetime of cosmic rays in the galaxy decreases with energy. Measurements of radioactive "clock" isotopes in the low energy cosmic radiation are consistent with a lifetime in the galaxy of about 15 Myr [14].

The spectrum of electrons and positrons incident at the top of the atmosphere is steeper than the spectra of protons and nuclei, as shown in Fig. 24.2. The positron fraction decreases from ~ 0.2 below 1 GeV [21–23] to ~ 0.1 around 2 GeV and to ~ 0.05 at the highest energies for which it is measured ($5 - 20$ GeV) [18]. This behavior refers to measurements made during solar cycles of positive magnetic polarity and at high geomagnetic latitude. Ref. 22 discusses the dependence of the positron fraction on solar cycle and Ref. 23 studies the geomagnetic effects.

The ratio of antiprotons to protons is $\sim 2 \times 10^{-4}$ [24] at around 10–20 GeV, and there is clear evidence [25] for the kinematic suppression at lower energy that is the signature of secondary antiprotons. The $\overline{p}/p$ ratio also shows a strong dependence on the phase and polarity of the solar cycle [26] in the opposite sense to that of the positron fraction. There is at this time no evidence for a significant primary component either of positrons or of antiprotons. No antihelium or antideuteron has been found in the cosmic radiation. The best current measured upper limit on the ratio antihelium/helium is approximately 7×10^{-7} [27]. The upper limit on the flux of antideuterons around 1 GeV/nucleon is approximately $2 \times 10^{-4}\,\mathrm{m}^2$ s sr GeV/nucleon [28].

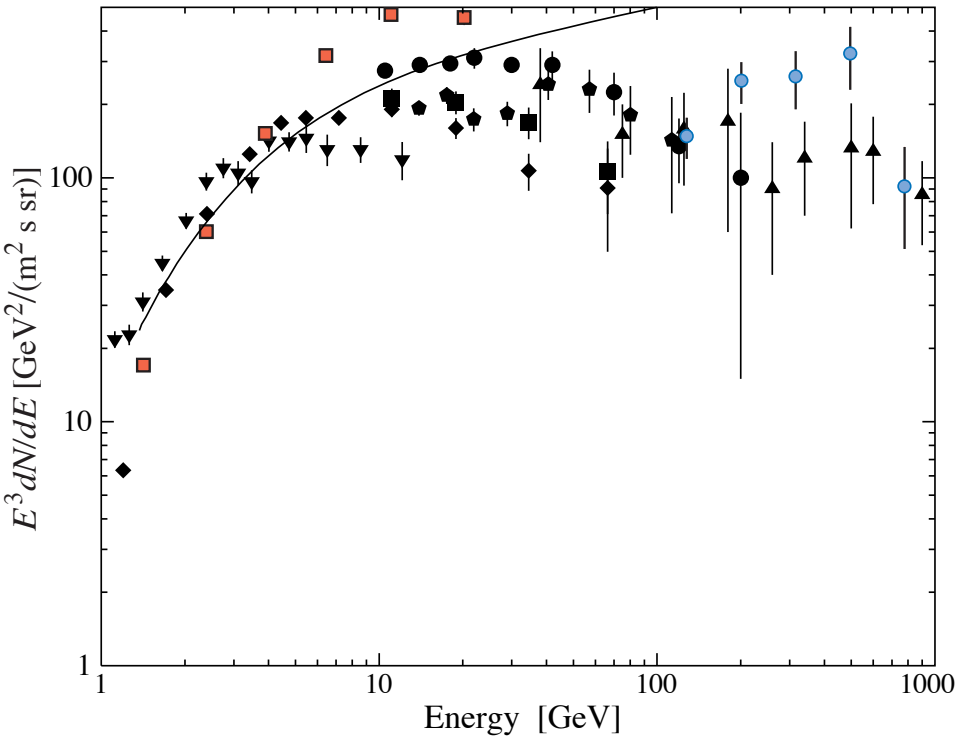

Figure 24.2: Differential spectrum of electrons plus positrons multiplied by E^3 (data from [15–22]) . The line shows the proton spectrum multiplied by 0.01.

24.2. Cosmic rays in the atmosphere

Figure 24.3 shows the vertical fluxes of the major cosmic ray components in the atmosphere in the energy region where the particles are most numerous (except for electrons, which are most numerous near their critical energy, which is about 81 MeV in air). Except for protons and electrons near the top of the atmosphere, all particles are produced in interactions of the primary cosmic rays in the air. Muons and neutrinos are products of the decay of charged mesons, while electrons and photons originate in decays of neutral mesons.

Most measurements are made at ground level or near the top of the atmosphere, but there are also measurements of muons and electrons from airplanes and balloons. Fig. 24.3 includes recent measurements of negative muons [29–32]. Since $\mu^+(\mu^-)$ are produced in association with $\nu_\mu(\overline{\nu}_\mu)$, the measurement of muons near the maximum of the intensity curve for the parent pions serves to calibrate the atmospheric ν_μ beam [33]. Because muons typically lose almost two GeV in passing through the atmosphere, the comparison near the production altitude is important for the sub-GeV range of $\nu_\mu(\overline{\nu}_\mu)$ energies.

The flux of cosmic rays through the atmosphere is described by a set of coupled cascade equations with boundary conditions at the top of the atmosphere to match the primary spectrum. Numerical or Monte Carlo calculations are needed to account accurately for decay and energy-loss processes, and for the energy-dependences of the cross sections and

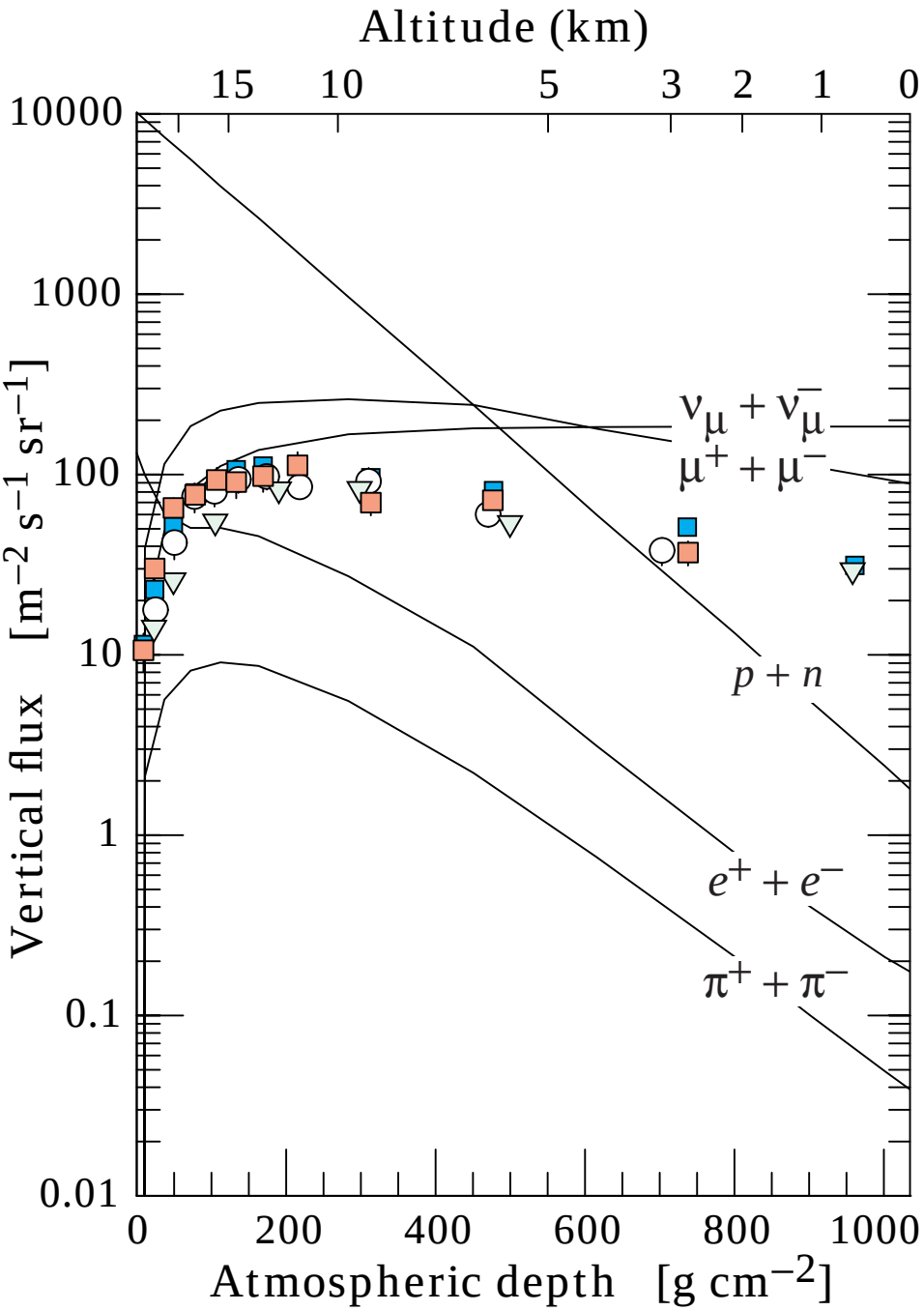

Figure 24.3: Vertical fluxes of cosmic rays in the atmosphere with $E > 1$ GeV estimated from the nucleon flux of Eq. (24.2). The points show measurements of negative muons with $E_\mu > 1$ GeV [29–32].

of the primary spectral index γ. Approximate analytic solutions are, however, useful in limited regions of energy [34,35]. For example, the vertical intensity of nucleons at depth

X (g cm^{-2}) in the atmosphere is given by

$$I_N(E, X) \approx I_N(E, 0)\, e^{-X/\Lambda} , \tag{24.3}$$

where Λ is the attenuation length of nucleons in air.

The corresponding expression for the vertical intensity of charged pions with energy $E_\pi \ll \epsilon_\pi = 115$ GeV is

$$I_\pi(E_\pi, X) \approx \frac{Z_{N\pi}}{\lambda_N} I_N(E_\pi, 0)\, e^{-X/\Lambda} \frac{X\, E_\pi}{\epsilon_\pi} . \tag{24.4}$$

This expression has a maximum at $X = \Lambda \approx 121 \pm 4$ g cm^{-2} [36], which corresponds to an altitude of 15 kilometers. The quantity $Z_{N\pi}$ is the spectrum-weighted moment of the inclusive distribution of charged pions in interactions of nucleons with nuclei of the atmosphere. The intensity of low-energy pions is much less than that of nucleons because $Z_{N\pi} \approx 0.079$ is small and because most pions with energy much less than the critical energy ϵ_π decay rather than interact.

24.3. Cosmic rays at the surface

24.3.1. ***Muons*** : Muons are the most numerous charged particles at sea level (see Fig. 24.3). Most muons are produced high in the atmosphere (typically 15 km) and lose about 2 GeV to ionization before reaching the ground. Their energy and angular distribution reflect a convolution of production spectrum, energy loss in the atmosphere, and decay. For example, 2.4 GeV muons have a decay length of 15 km, which is reduced to 8.7 km by energy loss. The mean energy of muons at the ground is ≈ 4 GeV. For GeV muons there is also a solar activity and a latitude effect that results from the geomagnetic effects. These two effects affect the GeV muon flux at the 10% level. The energy spectrum is almost flat below 1 GeV, steepens gradually to reflect the primary spectrum in the 10–100 GeV range, and steepens further at higher energies because pions with $E_\pi > \epsilon_\pi$ tend to interact in the atmosphere before they decay. Asymptotically ($E_\mu \gg 1$ TeV), the energy spectrum of atmospheric muons is one power steeper than the primary spectrum. The integral intensity of vertical muons above 1 GeV/c at sea level is ≈ 70 m^{-2}s^{-1}sr^{-1} [37,38], with recent measurements [39–41] tending to give lower normalization by 10-15%. Experimentalists are familiar with this number in the form $I \approx 1$ cm^{-2} min^{-1} for horizontal detectors.

The overall angular distribution of muons at the ground is $\propto \cos^2\theta$, which is characteristic of muons with $E_\mu \sim 3$ GeV. At lower energy the angular distribution becomes increasingly steep, while at higher energy it flattens, approaching a $\sec\theta$ distribution for $E_\mu \gg \epsilon_\pi$ and $\theta < 70°$.

An approximate extrapolation formula valid when muon decay is negligible ($E_\mu > 100/\cos\theta$ GeV), and the curvature of the Earth can be neglected ($\theta < 70°$) is

$$\frac{dN_\mu}{dE_\mu d\Omega} \approx \frac{0.14\, E_\mu^{-2.7}}{\text{cm}^2 \text{ s sr GeV}}$$

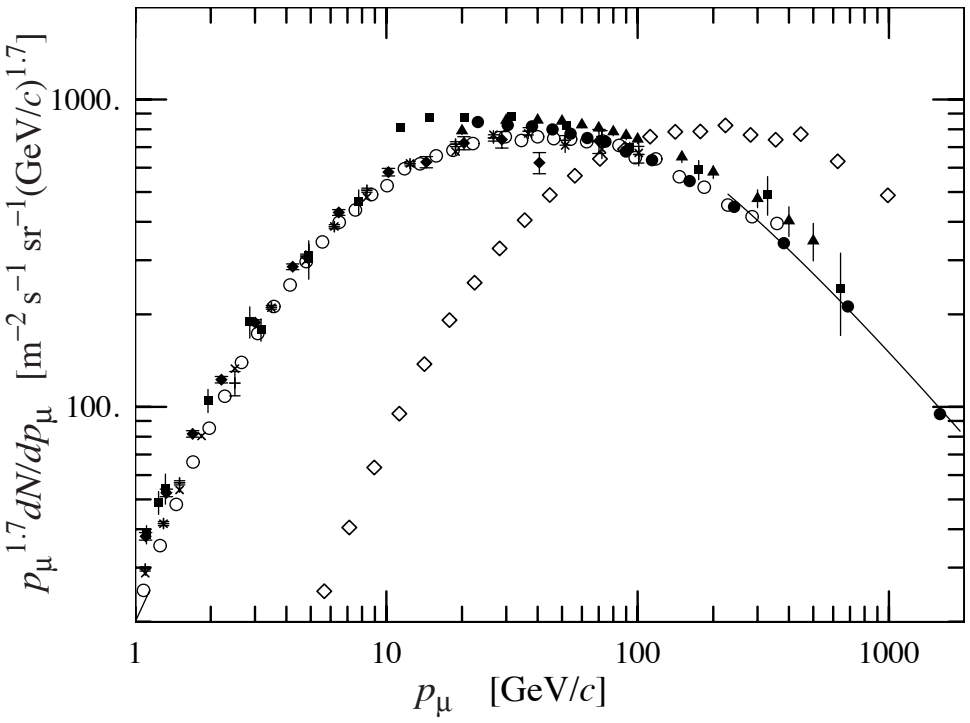

Figure 24.4: Spectrum of muons at $\theta = 0°$ (⧫ [37], ■ [42], ▼ [43], ▲ [44], ×, + [39], ○ [40] and (blakcircles) [41] and $\theta = 75°$ ◇ [45]) . The line plots the result from Eq. (24.5) for vertical showers.

$$\times \left\{ \frac{1}{1 + \dfrac{1.1 E_\mu \cos\theta}{115\,\mathrm{GeV}}} + \frac{0.054}{1 + \dfrac{1.1 E_\mu \cos\theta}{850\,\mathrm{GeV}}} \right\} , \tag{24.5}$$

where the two terms give the contribution of pions and charged kaons. Eq. (24.5) neglects a small contribution from charm and heavier flavors which is negligible except at very high energy [46].

Figure 24.4 shows the muon energy spectrum at sea level for two angles. At large angles low energy muons decay before reaching the surface and high energy pions decay before they interact, thus the average muon energy increases.

The muon charge ratio reflects the excess of π^+ over π^- and K^+ over K^- in the forward fragmentation region of proton initiated interactions together with the fact that there are more protons than neutrons in the primary spectrum. The increase with energy of μ^+/μ^- shown in Fig. 24.5 reflects the increasing importance of kaons in the TeV range [47], and indicates a significant contribution of associated production by cosmic-ray protons ($p \to \Lambda + K^+$). The same process is even more important for atmospheric neutrinos at high energy.

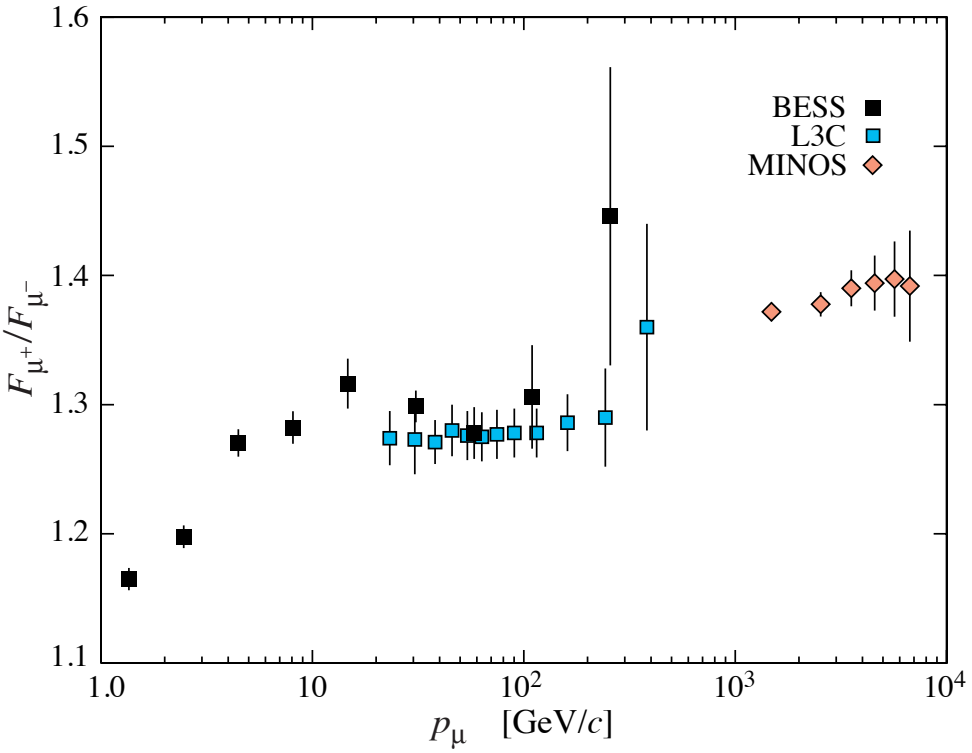

Figure 24.5: Muon charge ratio as a function of the muon momentum from Refs. [40,41,47,48].

24.3.2. ***Electromagnetic component*** : At the ground, this component consists of electrons, positrons, and photons primarily from electromagnetic cascades initiated by decay of neutral and charged mesons. Muon decay is the dominant source of low-energy electrons at sea level. Decay of neutral pions is more important at high altitude or when the energy threshold is high. Knock-on electrons also make a small contribution at low energy [49]. The integral vertical intensity of electrons plus positrons is very approximately 30, 6, and 0.2 $\mathrm{m^{-2}s^{-1}sr^{-1}}$ above 10, 100, and 1000 MeV respectively [38,50], but the exact numbers depend sensitively on altitude, and the angular dependence is complex because of the different altitude dependence of the different sources of electrons [49–51]. The ratio of photons to electrons plus positrons is approximately 1.3 above a GeV and 1.7 below the critical energy [51].

24.3.3. ***Protons*** : Nucleons above 1 GeV/c at ground level are degraded remnants of the primary cosmic radiation. The intensity is approximately represented by Eq. (24.3), with the replacement $X \to X/\cos\theta$ for $\theta < 70°$. At sea level, about 1/3 of the nucleons in the vertical direction are neutrons (up from $\approx 10\%$ at the top of the atmosphere as the n/p ratio approaches equilibrium). The integral intensity of vertical protons above 1 GeV/c at sea level is ≈ 0.9 $\mathrm{m^{-2}s^{-1}sr^{-1}}$ [38,52].

24.4. Cosmic rays underground

Only muons and neutrinos penetrate to significant depths underground. The muons produce tertiary fluxes of photons, electrons, and hadrons.

24.4.1. ***Muons*** : As discussed in Section 27.6 of this *Review*, muons lose energy by ionization and by radiative processes: bremsstrahlung, direct production of e^+e^- pairs, and photonuclear interactions. The total muon energy loss may be expressed as a function of the amount of matter traversed as

$$-\frac{dE_\mu}{dX} \;=\; a + b\,E_\mu \;, \tag{24.6}$$

where a is the ionization loss and b is the fractional energy loss by the three radiation processes. Both are slowly varying functions of energy. The quantity $\epsilon \equiv a/b$ (≈ 500 GeV in standard rock) defines a critical energy below which continuous ionization loss is more important than radiative losses. Table 24.2 shows a and b values for standard rock as a function of muon energy. The second column of Table 24.2 shows the muon range in standard rock ($A = 22$, $Z = 11$, $\rho = 2.65$ g cm^{-3}). These parameters are quite sensitive to the chemical composition of the rock, which must be evaluated for each experimental location.

Table 24.2: Average muon range R and energy loss parameters calculated for standard rock [53]. Range is given in km-water-equivalent, or 10^5 g cm^{-2}.

E_μ	R	a	$b_{\rm brems}$	$b_{\rm pair}$	$b_{\rm nucl}$	$\sum b_i$	$\sum b$(ice)
GeV	km.w.e.	MeV g^{-1} cm^2	———	10^{-6} g^{-1} cm^2		———	
10	0.05	2.17	0.70	0.70	0.50	1.90	1.66
100	0.41	2.44	1.10	1.53	0.41	3.04	2.51
1000	2.45	2.68	1.44	2.07	0.41	3.92	3.17
10000	6.09	2.93	1.62	2.27	0.46	4.35	3.78

The intensity of muons underground can be estimated from the muon intensity in the atmosphere and their rate of energy loss. To the extent that the mild energy-dependence of a and b can be neglected, Eq. (24.6) can be integrated to provide the following relation between the energy $E_{\mu,0}$ of a muon at production in the atmosphere and its average energy E_μ after traversing a thickness X of rock (or ice or water):

$$E_\mu \;=\; (E_{\mu,0} + \epsilon)\, e^{-bX} \;-\; \epsilon \;. \tag{24.7}$$

Especially at high energy, however, fluctuations are important and an accurate calculation requires a simulation that accounts for stochastic energy-loss processes [54].

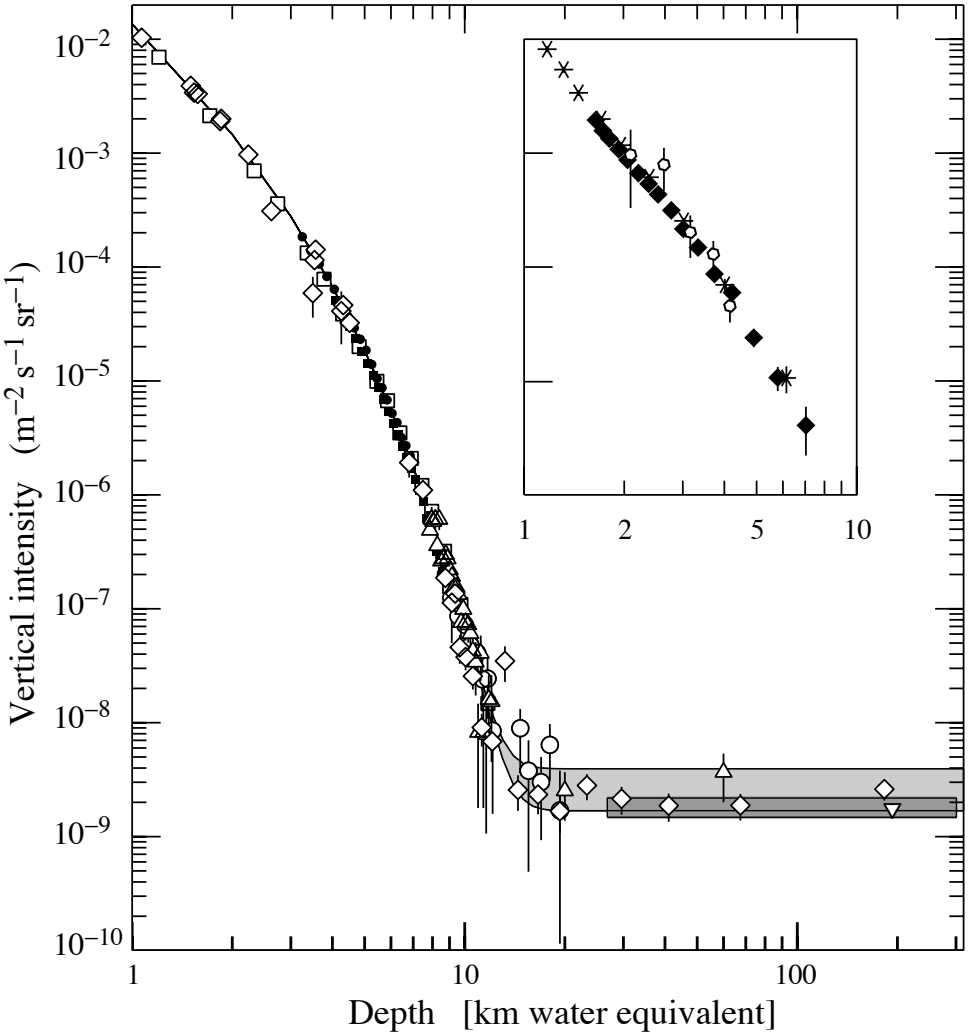

Figure 24.6: Vertical muon intensity vs depth (1 km.w.e. = 10^5 g cm^{-2} of standard rock). The experimental data are from: ◊: the compilations of Crouch [55], □: Baksan [59], ○: LVD [60], •: MACRO [61], ■: Frejus [62], and △SNO [63]. The shaded area at large depths represents neutrino-induced muons of energy above 2 GeV. The upper line is for horizontal neutrino-induced muons, the lower one for vertically upward muons.

There are two depth regimes for Eq. (24.7). For $X \ll b^{-1} \approx 2.5$ km water equivalent, $E_{\mu,0} \approx E_\mu(X) + aX$, while for $X \gg b^{-1}$ $E_{\mu,0} \approx (\epsilon + E_\mu(X)) \exp(bX)$. Thus at shallow depths, the differential muon energy spectrum is approximately constant for $E_\mu < aX$, and steepens to reflect the surface muon spectrum for $E_\mu > aX$, whereas for $X > 2.5$ km.w.e., the differential spectrum underground is again constant for small muon energies but steepens to reflect the surface muon spectrum for $E_\mu > \epsilon \approx 0.5$ TeV. In the deep regime, the shape is independent of depth, although the intensity decreases

exponentially with depth. In general the muon spectrum at slant depth X is

$$\frac{dN_\mu(X)}{dE_\mu} = \frac{dN_\mu}{dE_{\mu,0}} \frac{dE_{\mu,0}}{dE_\mu} = \frac{dN_\mu}{dE_{\mu,0}} e^{bX} \ , \tag{24.8}$$

where $E_{\mu,0}$ is the solution of Eq. (24.7) in the approximation neglecting fluctuations.

Fig. 24.6 shows the vertical muon intensity versus depth. In constructing this "depth-intensity curve," each group has taken account of the angular distribution of the muons in the atmosphere, the map of the overburden at each detector, and the properties of the local medium in connecting measurements at various slant depths and zenith angles to the vertical intensity. Use of data from a range of angles allows a fixed detector to cover a wide range of depths. The flat portion of the curve is due to muons produced locally by charged-current interactions of ν_μ. The inset shows the vertical intensity curve for water and ice published in Refs. [56–58]. It is not as steep as the one for rock because of the lower muon energy loss in water.

24.4.2. ***Neutrinos*** : Because neutrinos have small interaction cross sections, measurements of atmospheric neutrinos require a deep detector to avoid backgrounds. There are two types of measurements: contained (or semi-contained) events, in which the vertex is determined to originate inside the detector, and neutrino-induced muons. The latter are muons that enter the detector from zenith angles so large (*e.g.*, nearly horizontal or upward) that they cannot be muons produced in the atmosphere. In neither case is the neutrino flux measured directly. What is measured is a convolution of the neutrino flux and cross section with the properties of the detector (which includes the surrounding medium in the case of entering muons).

Contained and semi-contained events reflect neutrinos in the sub-GeV to multi-GeV region, where the product of increasing cross section and decreasing flux is maximum. In the GeV region, the neutrino flux and its angular distribution depend on the geomagnetic location of the detector and, to a lesser extent, on the phase of the solar cycle. Naively, we expect $\nu_\mu/\nu_e = 2$ from counting neutrinos of the two flavors coming from the chain of pion and muon decay. This ratio is only slightly modified by the details of the decay kinematics, but the fraction of electron neutrinos gradually decreases above a GeV as parent muons begin to reach the ground before decaying. Experimental measurements have to account for the ratio of $\overline{\nu}/\nu$, which have cross sections different by a factor of 3 in this energy range. In addition, detectors generally have different efficiencies for detecting muon neutrinos and electron neutrinos, which need to be accounted for in comparing measurements with expectation. Fig. 24.7 shows the distributions of the visible energy in the Super-Kamiokande detector [64] for electron-like and muon-like charged current neutrino interactions. Contrary to expectation, the numbers of the two classes of events are similar rather than different by a factor of two. The exposure for the data sample shown here is 1489 days. The falloff of the muon-like events at high energy is a consequence of the poor containment for high energy muons. Corrections for detection efficiencies and backgrounds are, however, insufficient to account for the large difference from the expectation [65,66].

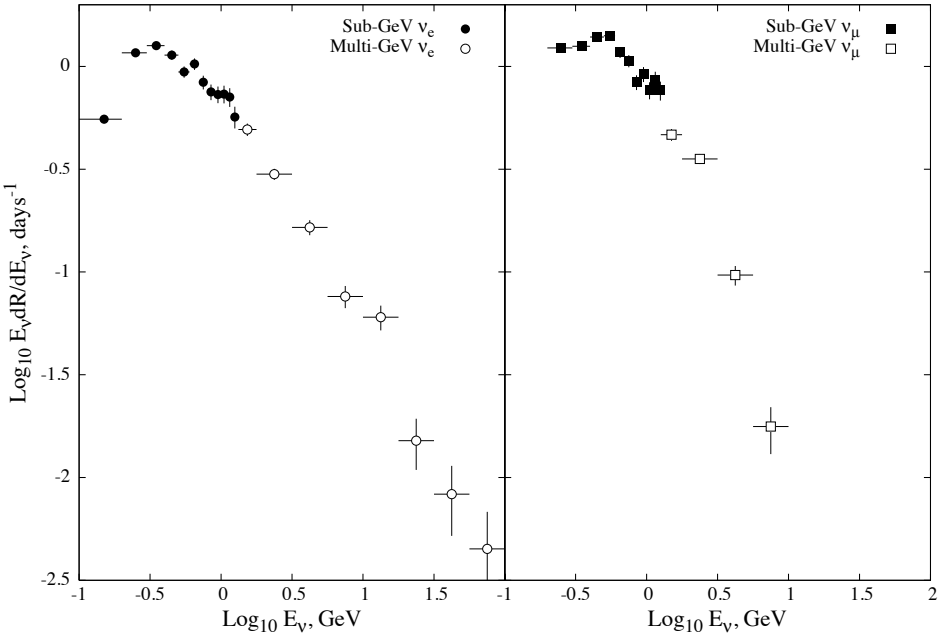

Figure 24.7: Sub-GeV and multi-GeV neutrino interactions from SuperKamiokande [64]. The plot shows the spectra of visible energy in the detector.

Two well-understood properties of atmospheric cosmic rays provide a standard for comparison of the measurements of atmospheric neutrinos. These are the "$\sec\theta$ effect" and the "east-west effect" [67]. The former refers originally to the enhancement of the flux of > 10 GeV muons (and neutrinos) at large zenith angles, because the parent pions propagate more in the low density upper atmosphere where decay is enhanced relative to interaction. For neutrinos from muon decay, the enhancement near the horizontal becomes important for $E_\nu > 1$ GeV, and arises mainly from the increased pathlength through the atmosphere for muon decay in flight. Fig. 24.8 from Ref. 64 shows a comparison between measurement and expectation for the zenith angle dependence of multi-GeV electron-like (mostly ν_e) and muon-like (mostly ν_μ) events separately. The ν_e show an enhancement near the horizontal and approximate equality for nearly upward ($\cos\theta \approx -1$) and nearly downward ($\cos\theta \approx 1$) events. There is, however, a very significant deficit of upward ($\cos\theta < 0$) ν_μ events, which have long pathlengths comparable to the radius of the Earth. This pattern has been interpreted as evidence for oscillations involving muon neutrinos [68]. (See the article on neutrino properties in this *Review*.) Including three dimensional effects in the calculation of atmospheric neutrinos may change somewhat the expected angular distributions of neutrinos at low energy [69], but it does not change the fundamental expectation of up-down symmetry, which is the basis of the evidence for oscillations.

Muons that enter the detector from outside after production in charged-current interactions of neutrinos naturally reflect a higher energy portion of the neutrino spectrum than contained events, because the muon range increases with energy as well as the cross section. The relevant energy range is $\sim 10 < E_\nu < 1000$ GeV, depending

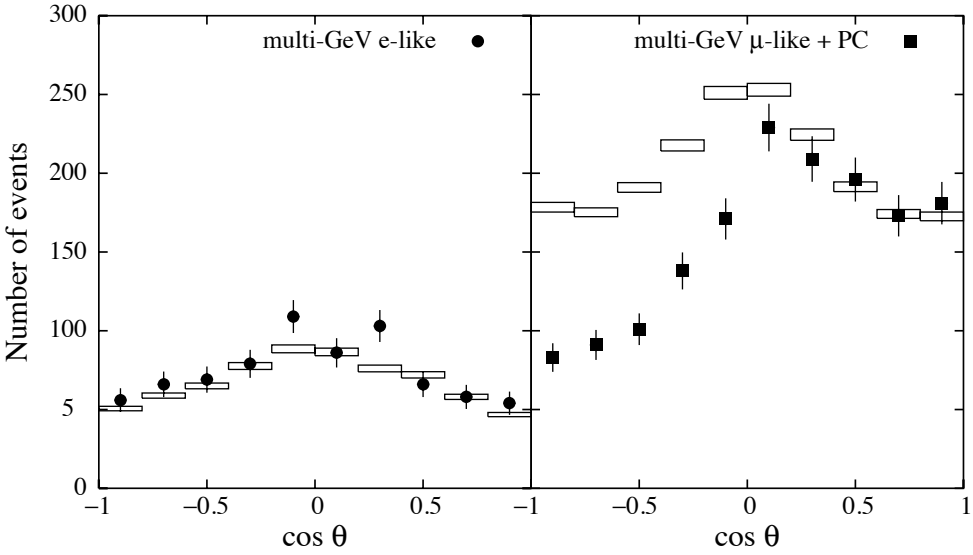

Figure 24.8: Zenith-angle dependence of multi-GeV neutrino interactions from SuperKamiokande [64]. The shaded boxes show the expectation in the absence of any oscillations.

Table 24.3: Measured fluxes (10^{-13} cm^{-2} s^{-1} sr^{-1}) of neutrino-induced muons as a function of the effective minimum muon energy E_μ.

$E_\mu >$	1 GeV	1 GeV	1 GeV	2 GeV	3 GeV	3 GeV
Ref.	CWI [70]	Baksan [71]	MACRO [72]	IMB [73]	Kam [74]	SuperK [75]
F_μ	2.17±0.21	2.77±0.17	2.29 ± 0.15	2.26±0.11	1.94±0.12	1.74±0.07

somewhat on angle. Neutrinos in this energy range show a $\sec\theta$ effect similar to muons (see Eq. (24.5)). This causes the flux of horizontal neutrino-induced muons to be approximately a factor two higher than the vertically upward flux. The upper and lower edges of the horizontal shaded region in Fig. 24.6 correspond to horizontal and vertical intensities of neutrino-induced muons. Table 24.3 gives the measured fluxes of upward-moving neutrino-induced muons averaged over the lower hemisphere. Generally the definition of minimum muon energy depends on where it passes through the detector. The tabulated effective minimum energy estimates the average over various accepted trajectories.

24.5. Air showers

So far we have discussed inclusive or uncorrelated fluxes of various components of the cosmic radiation. An air shower is caused by a single cosmic ray with energy high enough for its cascade to be detectable at the ground. The shower has a hadronic core, which acts as a collimated source of electromagnetic subshowers, generated mostly from $\pi^0 \to \gamma\,\gamma$ decays. The resulting electrons and positrons are the most numerous particles in the shower. The number of muons, produced by decays of charged mesons, is an order of magnitude lower. Air showers spread over a large area on the ground, and arrays of detectors operated for long times, are useful for studying cosmic rays with primary energy $E_0 > 100$ TeV, where the low flux makes measurements with small detectors in balloons and satellites difficult.

Greisen [76] gives the following approximate expressions for the numbers and lateral distributions of particles in showers at ground level. The total number of muons N_μ with energies above 1 GeV is

$$N_\mu(> 1\ \mathrm{GeV}) \;\approx\; 0.95 \times 10^5 \left(N_e/10^6\right)^{3/4} \;, \tag{24.9}$$

where N_e is the total number of charged particles in the shower (not just $e^\pm$). The number of muons per square meter, ρ_μ, as a function of the lateral distance r (in meters) from the center of the shower is

$$\rho_\mu = \frac{1.25\,N_\mu}{2\pi\,\Gamma(1.25)} \left(\frac{1}{320}\right)^{1.25} r^{-0.75} \left(1 + \frac{r}{320}\right)^{-2.5} \;, \tag{24.10}$$

where Γ is the gamma function. The number density of charged particles is

$$\rho_e = C_1(s, d, C_2)\, x^{(s-2)}(1+x)^{(s-4.5)}(1 + C_2 x^d) \;. \tag{24.11}$$

Here s, d, and C_2 are parameters in terms of which the overall normalization constant $C_1(s, d, C_2)$ is given by

$$\begin{aligned} C_1(s, d, C_2) = \frac{N_e}{2\pi r_1^2} \,[\, & B(s, 4.5 - 2s) \\ & + C_2\, B(s + d,\, 4.5 - d - 2s)]^{-1} \;, \end{aligned} \tag{24.12}$$

where $B(m, n)$ is the beta function. The values of the parameters depend on shower size (N_e), depth in the atmosphere, identity of the primary nucleus, *etc.* For showers with $N_e \approx 10^6$ at sea level, Greisen uses $s = 1.25$, $d = 1$, and $C_2 = 0.088$. Finally, x is r/r_1, where r_1 is the Molière radius, which depends on the density of the atmosphere and hence on the altitude at which showers are detected. At sea level $r_1 \approx 78$ m. It increases with altitude as the air density decreases.

The lateral spread of a shower is determined largely by Coulomb scattering of the many low-energy electrons and is characterized by the Molière radius. The lateral spread

of the muons (ρ_μ) is larger and depends on the transverse momenta of the muons at production, as well as multiple scattering.

There are large fluctuations in development from shower to shower, even for showers of the same energy and primary mass—especially for small showers, which are usually well past maximum development when observed at the ground. Thus the shower size N_e and primary energy E_0 are only related in an average sense, and even this relation depends on depth in the atmosphere. One estimate of the relation is [77]

$$E_0 \sim 3.9 \times 10^6 \text{ GeV } (N_e/10^6)^{0.9} \tag{24.13}$$

for vertical showers with $10^{14} < E < 10^{17}$ eV at 920 g cm^{-2} (965 m above sea level). As E_0 increases, the shower maximum (on average) moves down into the atmosphere and the relation between N_e and E_0 changes. Moreover, because of fluctuations, N_e as a function of E_0 is not correctly obtained by inverting Eq. (24.13). At the maximum of shower development, there are approximately 2/3 particles per GeV of primary energy.

There are three types of air shower detectors: shower arrays that study the shower size N_e and the lateral distribution on the ground, Cherenkov detectors that detect the Cherenkov radiation emitted by the charged particles of the shower, and fluorescence detectors that study the nitrogen fluorescence excited by the charged particles in the shower. The fluorescence light is emitted isotropically so the showers can be observed from the side. Detailed simulations and cross-calibrations between different types of detectors are necessary to establish the primary energy spectrum from air-shower experiments.

Figure 24.9 shows the "all-particle" spectrum. The differential energy spectrum has been multiplied by $E^{2.7}$ in order to display the features of the steep spectrum that are otherwise difficult to discern. The steepening that occurs between 10^{15} and 10^{16} eV is known as the *knee* of the spectrum. The feature around 10^{19} eV is called the *ankle* of the spectrum.

Measurements with small air shower experiments in the knee region differ by as much as a factor of two, indicative of systematic uncertainties in interpretation of the data. (For a review see Ref. 78.) Newer data sets are listed below. In establishing the spectrum shown in Fig. 24.9, efforts have been made to minimize the dependence of the analysis on the primary composition. Ref. 79 uses an unfolding procedure to obtain the spectra of the individual components, giving a result for the all-particle spectrum between 10^{15} and 10^{17} eV that lies toward the upper range of the data shown in Fig. 24.9. In the energy range above 10^{17} eV, the fluorescence technique [81] is particularly useful, because it can establish the primary energy in a model-independent way by observing most of the longitudinal development of each shower, from which E_0 is obtained by integrating the energy deposition in the atmosphere. The result, however, depends strongly on the light absorption in the atmosphere and the calculation of the detector's aperture.

Assuming the cosmic ray spectrum below 10^{18} eV is of galactic origin, the *knee* could reflect the fact that most cosmic accelerators in the galaxy have reached their maximum energy. Some types of expanding supernova remnants, for example, are estimated not to be able to accelerate protons above energies in the range of 10^{15} eV. Effects of propagation and confinement in the galaxy [82] also need to be considered.

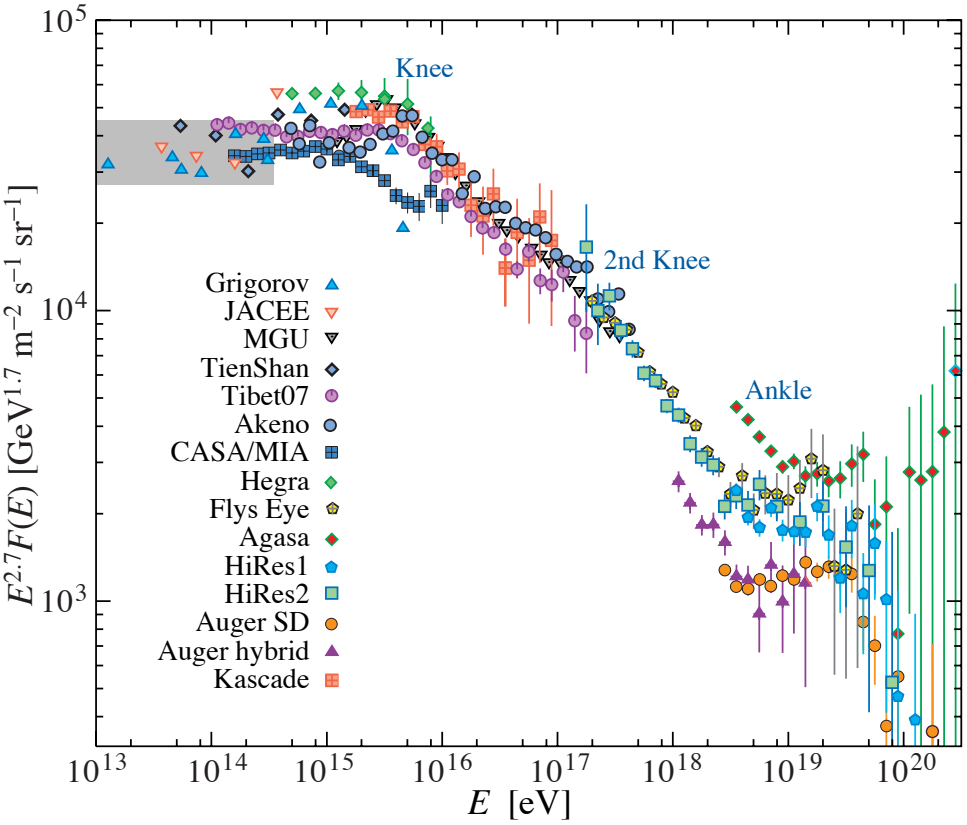

Figure 24.9: The all-particle spectrum from air shower measurements. The shaded area shows the range of the direct cosmic ray spectrum measurements.

Concerning the ankle, one possibility is that it is the result of a higher-energy population of particles overtaking a lower-energy population, for example, an extragalactic flux beginning to dominate over the galactic flux (*e.g.*, Ref. 81). Another possibility is that the dip structure in the region of the ankle is due to $\gamma p \to e^+ + e^-$ energy losses of extragalactic protons on the 2.7 K cosmic microwave radiation (CMB) [84]. This dip structure has been cited as a robust signature of both the protonic and extragalactic nature of the highest energy cosmic rays [83]. If this interpretation is correct, then the end of the galactic cosmic ray spectrum would be at an energy lower than 10^{18} eV, consistent with the maximum expected range of acceleration by supernova remnants. Energy-dependence of the composition from the knee through the ankle holds the key to discriminating between these two viewpoints.

If the cosmic ray flux above the second knee is cosmological in origin, there should be a rapid steepening of the spectrum (called the GZK feature) around 5×10^{19} eV, resulting from the onset of inelastic interactions of UHE cosmic rays with the cosmic microwave background [85,86]. Although all UHECR experiments have detected events of energy above 10^{20} eV [81], [87–89], the spectral shape above the ankle is still not well determined. The AGASA experiment [87] claimed 11 events above 10^{20} eV, while HiRes [88] detected only two. The Auger observatory presented spectra based on its

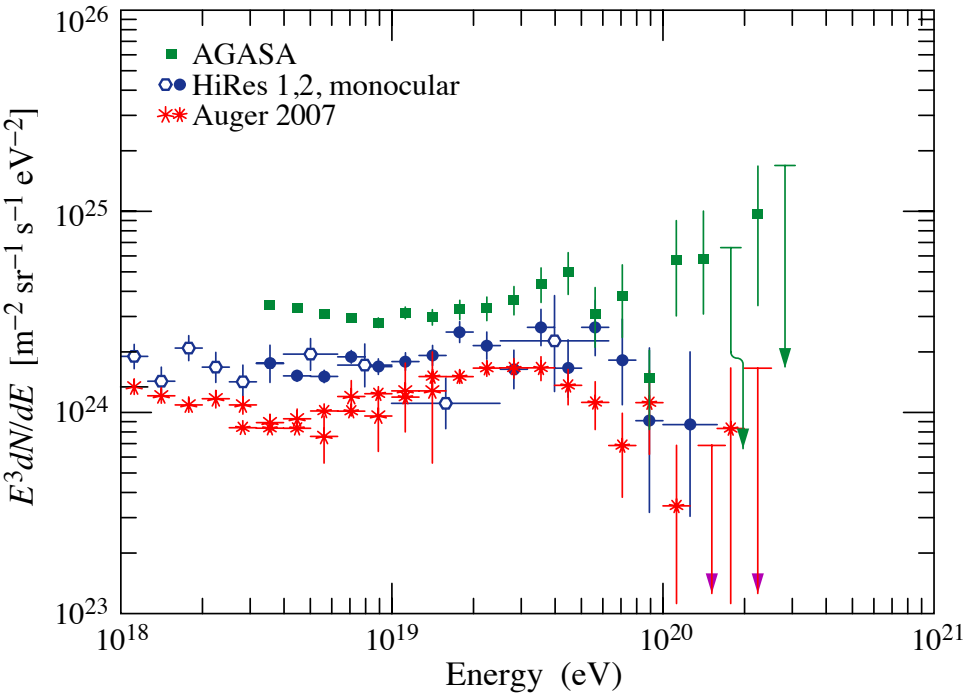

Figure 24.10: Expanded view of the highest energy portion of the cosmic-ray spectrum. ■ [87] (AGASA), ○● [88] (HiRes1,2 monocular), ∗ [89, 90] (Auger).

surface detector [89] and on events detected in hybrid mode [90], *i.e.*, with both the surface and the fluorescence detectors. The HiRes and Auger spectra show a significant steepening of the cosmic ray spectrum above 3-5×10^{19} eV, which is consistent with the onset of inelastic interactions with astrophysical photon fields, mostly the CMB [85,86].

Figure 24.10 gives an expanded view of the high energy end of the spectrum, showing only the more recent experiments. (See Ref. 91 for a recent review of all data about 10^{17} eV.) This figure and the previous one have shown the differential flux multiplied by a power of the energy, a procedure that enables one to see structure in the spectrum more clearly, but amplifies small systematic differences in energy assignments into sizable normalization differences. All existing experiments are actually consistent in normalization, if one takes quoted systematic errors in the energy scales into account. However, the continued power law type of flux beyond the GZK cutoff claimed by the AGASA experiment is not supported by the HiRes and Auger data. In November 2007 the Auger Collaboration reported [92] a correlation of the arrival directions of the highest energy cosmic rays with active galactic nuclei (AGN) at distance less than 75 Mpc. Twenty of 27 events with energy above 6×10^{19} eV arrive at an angle less than 3.1° from the position of a nearby AGN.

References:

1. M. Boezio *et al.*, Astropart. Phys. **19**, 583 (2003).
2. AMS Collaboration, Phys. Lett. **B490**, 27 (2000); Phys. Lett. **B494**, 193 (2000).
3. T. Sanuki *et al.*, Astrophys. J. **545**, 1135 (2000).
4. S. Haino *et al.*, Phys. Lett. **B594**, 35 (2004).
5. CREAM Collaboration, *Proc. 30th Int. Cosmic Ray Conf.,* (Merida, Yucatan, 2007), paper 0301.
6. J.J. Engelmann *et al.*, Astron. & Astrophys. **233**, 96 (1990).
7. D. Müller *et al.*, Ap J, **374**, 356 (1991).
8. P.J. Boyle *et al.*, Ap J submitted. See also P.J. Boyle *et al.*, *Proc. 30th Int. Cosmic Ray Conf.,* (Merida, Yucatan, 2007), paper 1192.
9. A.D. Panov *et al.*, Bull Russian Acad of Science, Physics, **71**, 494 (2007).
10. V.A. Derbina *et al.*, Astrophys. J. **628**, L41 (2005).
11. K. Asakimori *et al.*(JACEE Collaboration), Ap J, **502**, 278 (1998).
12. HESS Collaboration (F. Aharonian *et al.*), Phys. Rev. **D75**, 042004 (2007).
13. A.W. Strong *et al.*, Ann. Rev. Nucl. and Part. Sci. **157**, 285 (2007).
14. N.E. Yanasak *et al.*, Ap J, **563**, 768 (2001).
15. K.K. Tang, Astrophys. J. **278**, 881 (1984).
16. D. Müller & J. Tang, Astrophys. J. **312**, 183 (1987).
17. J. Nishimura Advances in Space Research **19**, 711 (1997).
18. M.A. DuVernois *et al.*, Astrophys. J. **559**, 296 (2000).
19. S. Torii *et al.*, Astrophys. J. **559**, 973 (2001).
20. K. Yoshida *et al.*, *Proc. 30th Int. Cosmic Ray Conf.,* (Merida, Yucatan, 2007), paper 0892.
21. M. Boezio *et al.*, Astrophys. J. **552**, 635 (2000).
22. J. Clem & P. Evenson, JGR 109 A07107 (2004).
23. J. Alcaraz *et al.*, Phys. Lett. **B484**, 10 (2000).
24. A.S. Beach *et al.*, Phys. Rev. Lett. **87**, 271101 (2001).
25. A. Yamamoto *et al.*, *Adv. Space Research* (2007) in press.
26. Y. Asaoka *et al.*, Phys. Rev. Lett. **88**, 51101 (2002).
27. M. Sasaki *et al.*, Nucl. Phys. **B113**, (Proc. Suppl.) 202 (2002).
28. H. Fuke *et al.*, Phys. Rev. Lett. **95**, 081101 (2005).
29. R. Bellotti *et al.*, Phys. Rev. **D53**, 35 (1996).
30. R. Bellotti *et al.*, Phys. Rev. **D60**, 052002 (1999).
31. M. Boezio *et al.*, Phys. Rev. **D62**, 032007 (2000).
32. S. Coutu *et al.*, Phys. Rev. **D62**, 032001 (2000).
33. T. Sanuki *et al.*, Phys. Rev. **D75**, 043005 (2007).
34. T.K. Gaisser, *Cosmic Rays and Particle Physics*, Cambridge University Press (1990).
35. P. Lipari, Astropart. Phys. **1**, 195 (1993).
36. E. Mocchiutto *et al.*, in *Proc. 28th Int. Cosmic Ray Conf.*, Tsukuba, 1627 (2003).
37. M.P. De Pascale *et al.*, J. Geophys. Res. **98**, 3501 (1993).
38. P.K.F. Grieder, *Cosmic Rays at Earth*, Elsevier Science (2001).
39. J. Kremer *et al.*, Phys. Rev. Lett. **83**, 4241 (1999).
40. BESS Collaboration (S. Haino *et al.*), Phys. Lett. **B527**, 35 (2004).

41. L3+C Collaboration (P. Archard *et al.*), Phys. Lett. **B598**, 15 (2004).
42. O.C. Allkofer, K. Carstensen, and W.D. Dau, Phys. Lett. **B36**, 425 (1971).
43. B.C. Rastin, J. Phys. **G10**, 1609 (1984).
44. C.A. Ayre *et al.*, J. Phys. **G1**, 584 (1975).
45. H. Jokisch *et al.*, Phys. Rev. **D19**, 1368 (1979).
46. C.G.S. Costa, Astropart. Phys. **16**, 193 (2001).
47. The MINOS Collaboration (P. Adamson *et al.*), Phys. Rev. **D76**, 052003 (2007).
48. M. Unger *et al.* (L3 Collab.), Inter. J. Mod. Phys. **A20**, 6928 (2005).
49. S. Hayakawa, *Cosmic Ray Physics*, Wiley, Interscience, New York (1969).
50. R.R. Daniel and S.A. Stephens, Revs. Geophysics & Space Sci. **12**, 233 (1974).
51. K.P. Beuermann and G. Wibberenz, Can. J. Phys. **46**, S1034 (1968).
52. I.S. Diggory *et al.*, J. Phys. **A7**, 741 (1974).
53. D.E. Groom, N.V. Mokhov, and S.I. Striganov, "Muon stopping-power and range tables," Atomic Data and Nuclear Data Tables, **78**, 183 (2001).
54. P. Lipari and T. Stanev, Phys. Rev. **D44**, 3543 (1991).
55. M. Crouch, in *Proc. 20th Int. Cosmic Ray Conf.*, Moscow, **6**, 165 (1987).
56. I.A. Belolaptikov *et al.*, Astropart. Phys. **7**, 263 (1997).
57. J. Babson *et al.*, Phys. Rev. **D42**, 3613 (1990).
58. P. Desiati *et al.*, in *Proc. 28th Int. Cosmic Ray Conf.*, Tsukuba, 1373 (2003).
59. Yu.M. Andreev, V.I. Gurentzov, and I.M. Kogai, in *Proc. 20th Int. Cosmic Ray Conf.*, Moscow, **6**, 200 (1987).
60. M. Aglietta *et al.*, (LVD Collaboration), Astropart. Phys. **3**, 311 (1995).
61. M. Ambrosio *et al.*, (MACRO Collaboration), Phys. Rev. **D52**, 3793 (1995).
62. Ch. Berger *et al.*, (Frejus Collaboration), Phys. Rev. **D40**, 2163 (1989).
63. C. Waltham *et al.*, in *Proc. 27th Int. Cosmic Ray Conf.*, Hamburg, 991 (2001).
64. SuperKamiokande Collaboration (Y. Ashie *et al.*), Phys. Rev. **D71**, 112005 (2005).
65. G. Barr *et al.*, Phys. Rev. **D70**, 023006 (2004).
66. M. Honda *et al.*, Phys. Rev. **D75**, 096005 (2007).
67. T. Futagami *et al.*, Phys. Rev. Lett. **82**, 5194 (1999).
68. Y. Fukuda *et al.*, Phys. Rev. Lett. **81**, 1562 (1998).
69. G. Battistoni *et al.*, Astropart. Phys. **12**, 315 (2000).
70. F. Reines *et al.*, Phys. Rev. Lett. **15**, 429 (1965).
71. M.M. Boliev *et al.*, in *Proc. 3rd Int. Workshop on Neutrino Telescopes* (ed. Milla Baldo Ceolin), 235 (1991).
72. M. Ambrosio *et al.*, (MACRO) Phys. Lett. **B434**, 451 (1998). The number quoted for MACRO is the average over 90% of the lower hemisphere, $\cos\theta < -0.1$; see F. Ronga *et al.*, `hep-ex/9905025`.
73. R. Becker-Szendy *et al.*, Phys. Rev. Lett. **69**, 1010 (1992); *Proc. 25th Int. Conf. High-Energy Physics*, Singapore (eds. K.K. Phua and Y. Yamaguchi, World Scientific), 662 1991).
74. S. Hatakeyama *et al.*, Phys. Rev. Lett. **81**, 2016 (1998).
75. Y. Fukuda *et al.*, Phys. Rev. Lett. **82**, 2644 (1999).
76. K. Greisen, Ann. Rev. Nucl. Sci. **10**, 63 (1960).
77. M. Nagano *et al.*, J. Phys. **G10**, 1295 (1984).

78. S.P. Swordy *et al.*, Astropart. Phys. **18**, 129 (2002).
79. Kascade collaboration (T. Antoni *et al.*), Astropart. Phys. **24**, 1 (2005).
80. M. Amenomori *et al.*, *Proc. 30th Int. Cosmic Ray Conf.,* (Merida, Yucatan, 2007), paper 0277.
81. D.J. Bird *et al.*, Astrophys. J. **424**, 491 (1994).
82. V.S. Ptuskin *et al.*, Astron. & Astrophys. **268**, 726 (1993).
83. V.S. Berezinsky and S.I. Grigor'eva, Astron. & Astrophys. **199**, 1 (1988).
84. V. Berezinsky, A. Gazizov, and S. Grigorieva, Phys. Rev. **D74**, 043005 (2006).
85. K. Greisen, Phys. Rev. Lett. **16**, 748 (1966).
86. G.T. Zatsepin and V.A. Kuz'min, Sov. Phys. JETP Lett. **4**, 78 (1966).
87. The AGASA Collaboration (M. Takeda *et al.*), Astropart. Phys. **19**, 447 (2003).
88. R. Abbasi *et al.*, Phys. Lett. B619, 271 (2005) (see also `astro-ph/0703099`).
89. The Auger Collaboration (M. Roth *et al.*), in *Proc. 30th Int. Cosmic Ray Conf.,* Merida, paper 0313 (2007) (`arXiv:0706.2096`).
90. The Auger Collaboration (L. Perrone *et al.*), in *Proc. 30th Int. Cosmic Ray Conf.,* Merida, paper 0316 (2007) (`arXiv:0706.2643`).
91. D.R. Bergman & J.W. Belz, J. Phys. G (in press), `arXiv:0704.3721`.
92. The Auger Collaboration, Science **318**, 938 (2007).